

Diffusion Probabilistic Models for Graph-Structured Prediction

Hyosoon Jang¹ Sangwoo Mo² Sungsoo Ahn¹

Abstract

This paper studies graph-structured prediction for supervised learning on graphs with node-wise or edge-wise target dependencies. To solve this problem, recent works investigated combining graph neural networks (GNNs) with conventional structured prediction algorithms like conditional random fields. However, in this work, we pursue an alternative direction building on the recent successes of diffusion probabilistic models (DPMs). That is, we propose a new framework using DPMs to make graph-structured predictions. In the fully supervised setting, our DPM captures the target dependencies by iteratively updating each target estimate based on the estimates of nearby targets. We also propose a variational expectation maximization algorithm to train our DPM in the semi-supervised setting. Extensive experiments verify that our framework consistently outperforms existing neural structured prediction models on inductive and transductive node classification. We also demonstrate the competitive performance of our framework for algorithmic reasoning tasks.¹

1. Introduction

Supervised learning often involves predicting a set of targets that are related to one another through a graph structure. One example is classifying documents in citation networks (Sen et al., 2008). In this task, documents closely connected in the network, such as through citations, are more likely to belong to the same class. To solve this type of problem, structured prediction algorithms output a joint predictive distribution that considers the element-wise dependency between targets, as described by the given graph structure.

To this end, researchers have developed structured prediction frameworks such as conditional random fields (Lafferty et al., 2001, CRFs) or iterative classification algorithms (Chakrabarti et al., 1998, ICAs). CRFs model the output

¹POSTECH ²KAIST. Correspondence to: Sungsoo Ahn <sungsoo.ahn@postech.ac.kr>.

Preprint. Under review.

¹Code: <https://github.com/hsjang0/DPM-GSP>.

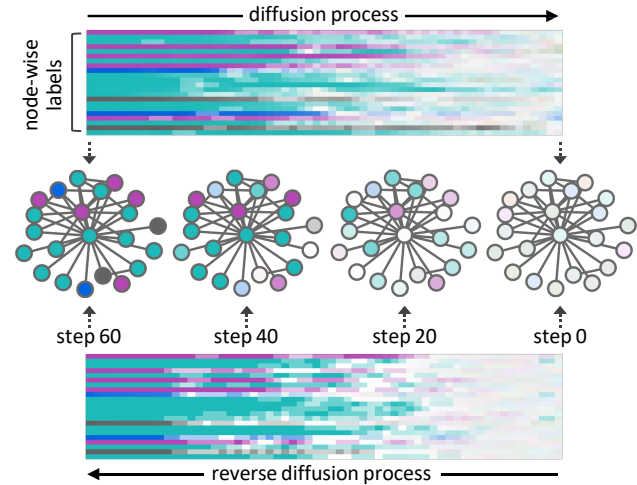


Figure 1. Illustration of our DPM solving a node classification problem. DPM makes a prediction by denoising a diffusion process on an input graph. Node color indicates the label type, and opacity is proportional to the likelihood of the true label in a prediction.

dependencies via Markov networks conditioned on inputs. ICAs recursively update predictions on each target using the past predictions of neighboring targets until convergence.

With the recent advent of graph neural networks (Kipf & Welling, 2016a; Xu et al., 2018, GNNs), researchers investigated combining GNNs with structured prediction algorithms (Ma et al., 2019b; Qu et al., 2019; Graber & Schwing, 2019; Qu et al., 2022). For example, Ma et al. (2019b); Qu et al. (2019; 2022) proposed to parameterize a CRF using GNNs. They differ by training the CRF using pseudo-likelihood or a GNN-based proxy. Next, Hang et al. (2021) proposed to aggregate multiple GNN predictions as an ICA.

In this work, we pursue an alternative research direction for GNN-based structured prediction. In particular, we propose to use the diffusion probabilistic model (Ho et al., 2020, DPM), which makes a prediction via iterative denoising of a diffusion process. We also propose a new variational expectation-maximization (EM) algorithm to train DPMs for semi-supervised settings. See Figure 1 for an illustration of our DPM for node classification. Our DPM expresses the target-wise dependencies via recursively updating a node-wise prediction using past predictions of neighboring nodes.

We advocate that using DPMs for the graph-structured prediction can exploit their extraordinary capability in learning highly structured data (Li et al., 2022; Chen et al., 2022b; Hoogeboom et al., 2022b). In particular, our DPM makes a prediction using a GNN-based reverse diffusion process. This allows structured prediction with a range of dependencies proportional to the number of diffusion steps. Such a dependency requires an impractically large number of layers to learn using other GNN-based deep generative models, e.g., graph variational autoencoder (Kipf & Welling, 2016b).

We design our variational EM to train DPMs in semi-supervised settings, e.g., transductive node classification. Primarily, we suggest two strategies for adapting variational EM to our problem. First, we use a buffer to stabilize the optimization. We also use manifold-constrained sampling (Chung et al., 2022) to sample from DPM conditioned on ground truth labels during the expectation step.

We extensively validate our method on eight inductive and eight transductive node classification problems constructed from ten datasets: DBLP (Tang et al., 2008), PPI (Zitnik & Leskovec, 2017), Pubmed, Cora and Citeseer (Yang et al., 2016), Photo and Computer (Shchur et al., 2018), and Cornell, Wisconsin, and Texas (Zhu et al., 2020). Our framework consistently outperforms the existing graph-structured prediction algorithms. We also show the superiority of our algorithm for graph algorithmic reasoning tasks that aim to predict the algorithmic outputs for edge copy, shortest path, and connected components (Du et al., 2022).

2. Related Work

Graph neural networks (GNNs). In recent years, GNNs have shown great success for graph representation learning (Kipf & Welling, 2016a; Hamilton et al., 2017; Veličković et al., 2017; Chamberlain et al., 2021). However, without additional modification, GNNs make unstructured predictions ignoring the dependencies between targets. For example, when predicting node-wise labels $\mathbf{y} = \{y_i : i \in \mathcal{V}\}$, GNNs output a predictive distribution $p_\theta(\mathbf{y})$ where the node-wise predictions are independent, i.e., $p_\theta(\mathbf{y}) = \prod_{i \in \mathcal{V}} p_\theta(y_i)$.

Structured prediction algorithms. Structured prediction algorithms aim to model the dependencies within the output space. One representative framework is conditional random fields (Sutton et al., 2012, CRFs), which output Markov random fields conditioned on the input. CRFs describe the dependencies between predictions using pair-wise potential functions. They have shown success in many applications, e.g., part-of-speech tagging (PVS & Karthik, 2007) and entity recognition (Patil et al., 2020). In another line of research, iterative classification algorithms (Neville & Jensen, 2000, ICAs) incorporate the target-wise dependencies via iterative message-passing updates between predictions.

Graph-structured prediction with GNNs. Recently, several works focus on combining deep neural networks with structured prediction algorithms (Belanger & McCallum, 2016; Graber et al., 2018; Garcia Satorras et al., 2019; Qu et al., 2019; Hang et al., 2021; Du et al., 2022; Qu et al., 2022). In particular, researchers have considered GNN-based graph-structured prediction for node classification (Qu et al., 2019; Hang et al., 2021; Qu et al., 2022). First, Qu et al. (2019) parameterize the potential functions of a CRF using a GNN and train the CRF using pseudo-likelihood maximization (Besag, 1975). As an alternative way to train the CRF, Qu et al. (2022) proposed a training scheme based on a GNN-based proxy for the potential functions. Both methods achieve superior performance by combining the expressive power of GNNs and the ability of CRFs to make graph-structured predictions. Hang et al. (2021) propose an ICA-based learning framework of GNNs that updates each node-wise prediction by aggregating previous predictions on neighboring nodes. Finally, Ma et al. (2019a) solves the problem with a generative framework that learn the joint distribution of node features, labels, and graph structure.

Diffusion probabilistic models (DPMs). Inspired by non-equilibrium thermodynamics, DPMs are deep generative models (Sohl-Dickstein et al., 2015) that learn to reverse a diffusion process and construct data from a noise distribution. Recent works demonstrated great success of DPMs in various domains, e.g., generating images (Dhariwal & Nichol, 2021), 3D shapes (Zhou et al., 2021), text (Li et al., 2022), and molecules (Hoogeboom et al., 2022b). In particular, researchers showed that DPMs even make predictions with complex structures, e.g., image segmentation (Chen et al., 2022b) and object detection (Chen et al., 2022a).

3. Diffusion Probabilistic Model for Graph-Structured Prediction (DPM-GSP)

In this section, we introduce our framework to use a diffusion probabilistic model for graph-structured prediction (DPM-GSP). We consider supervised learning on graphs where the task is to predict node-wise or edge-wise targets. We aim to make a graph-structured prediction that captures the target-wise dependencies characterized by a graph, e.g., in homogeneous graphs, neighboring nodes are more likely to be associated with similar targets (Wang & Zhang, 2006).

In the following, we describe our DPM-GSP for fully-supervised and semi-supervised node classification. Our algorithm is applicable to both transductive and inductive settings without modification, i.e., when the test input is seen or unseen during training. We remark that our DPM-GSP is not only capable of predicting node-wise targets, but can also be extended to predict edge-wise targets.

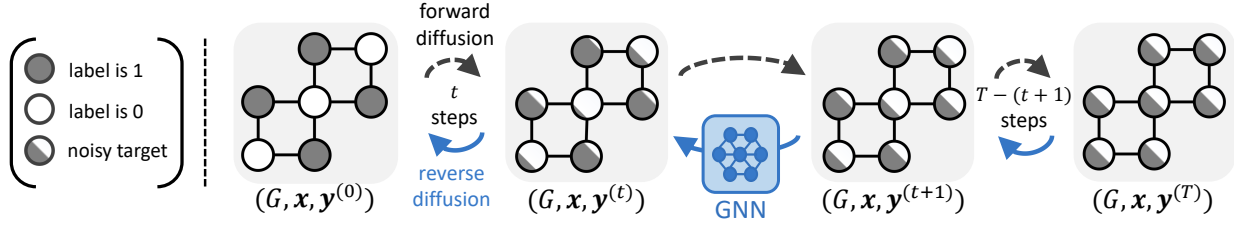


Figure 2. Overview of our DPM-GSP in the fully supervised setting. DPM-GSP predicts the noisy targets by iteratively updating the previous predictions with a GNN-based reverse diffusion process.

3.1. Fully supervised node classification

Here, we consider supervised learning on a graph G with attributes \mathbf{x} to predict targets \mathbf{y} . To be specific, the graph $G = (\mathcal{V}, \mathcal{E})$ consists of a node set \mathcal{V} and an edge set \mathcal{E} . We assume that the attributes and the targets are associated with nodes, i.e., $\mathbf{x} = \{x_i : i \in \mathcal{V}\}$ and $\mathbf{y} = \{y_i : i \in \mathcal{V}\}$.² If the targets \mathbf{y} are discrete, we relax them into an one-hot vector to yield continuous values.

Our DPM consists of forward and reverse diffusion processes, following the design of Ho et al. (2020). The fixed forward diffusion process iteratively injects noise into the targets until converging to a standard Gaussian distribution.³ Conversely, the GNN-based reverse diffusion process aims to reconstruct the targets from the standard Gaussian distribution, conditioned on a given graph. By construction, our GNN-based reverse diffusion process can express long-range dependencies without training very deep GNNs.⁴ We train the DPM to maximize the lower bound of the log-likelihood for the reverse diffusion process, with the ultimate goal of generating the correct targets from a given graph.

Forward diffusion process. Given a target $\mathbf{y}^{(0)} = \mathbf{y}$ and the number of diffusion steps T our forward diffusion process constructs a sequence of noisy targets $\mathbf{y}^{(1)}, \dots, \mathbf{y}^{(T)}$ using a fixed distribution $q(\cdot)$ defined as follows:

$$q(\mathbf{y}^{(1)}, \dots, \mathbf{y}^{(T)} | \mathbf{y}^{(0)}) = \prod_{t=1}^T q(\mathbf{y}^{(t)} | \mathbf{y}^{(t-1)}),$$

$$q(\mathbf{y}^{(t)} | \mathbf{y}^{(t-1)}) = \mathcal{N}(\mathbf{y}^{(t)}; \sqrt{\alpha_t} \mathbf{y}^{(t-1)}, \beta_t \mathbf{I}),$$

where \mathbf{I} is an identity matrix, β_1, \dots, β_T are fixed variance schedules, and $\alpha_t = 1 - \beta_t$. We set the variance schedule to promote $q(\mathbf{y}^{(T)} | \mathbf{y}^{(0)}) \approx \mathcal{N}(\mathbf{y}^{(T)}; \mathbf{0}, \mathbf{I})$ by setting $\beta_t < \beta_{t+1}$ for $t = 0, \dots, T-1$ and $\beta_T = 1$. We provide a detailed variance scheduling method in Appendix A.

Reverse diffusion process. Given an initial sample $\mathbf{y}^{(T)}$ sampled from $p(\mathbf{y}^{(T)}) = \mathcal{N}(\mathbf{y}^{(T)}; \mathbf{0}, \mathbf{I})$, the reverse dif-

fusion process $p_\theta(\mathbf{y}^{(0)}, \dots, \mathbf{y}^{(T-1)} | \mathbf{x}, \mathbf{y}^{(T)}, G)$ learns to reconstruct the forward diffusion process given by $q(\cdot)$. To be specific, it is formulated as follows:

$$p_\theta(\mathbf{y}^{(0)}, \dots, \mathbf{y}^{(T-1)} | \mathbf{y}^{(T)}) = \prod_{t=1}^T p_\theta(\mathbf{y}^{(t-1)} | \mathbf{y}^{(t)}),$$

$$p_\theta(\mathbf{y}^{(t-1)} | \mathbf{y}^{(t)}) = \mathcal{N}(\mathbf{y}^{(t-1)}; \boldsymbol{\mu}_\theta(\mathbf{x}, \mathbf{y}^{(t)}, G, t), \sigma_t^2 \mathbf{I}),$$

where we omit the conditional dependency of p_θ on graph G and attributes \mathbf{x} for simplicity of notation. We parameterize the denoised mean value $\boldsymbol{\mu}_\theta(\cdot)$ of $\mathbf{y}^{(t-1)}$ using a graph neural network (GNN). We provide a detailed description of the GNNs in Appendix A.

Training objective. We train our DPM to maximize the variational lower bound of the marginal log-likelihood $\log p_\theta(\mathbf{y}^{(0)})$. To this end, we minimize the simplified training objective defined as follows:

$$\mathcal{L} = \sum_{t=1}^T \frac{1}{\sigma_t^2} \mathbb{E}_{q(\mathbf{y}^{(t)} | \mathbf{y}^{(0)})} [\|\boldsymbol{\mu}_\theta(\mathbf{x}, \mathbf{y}^{(t)}, G, t) - \hat{\boldsymbol{\mu}}\|_2^2]. \quad (1)$$

Here, $\hat{\boldsymbol{\mu}}$ denotes average of the conditional distribution $q(\mathbf{y}^{(t-1)} | \mathbf{y}^{(t)}, \mathbf{y}^{(0)})$ that can be computed in a closed form. In practice, we optimize the residual from the mean value; the detailed description is in Appendix A.

Deterministic inference. We propose a deterministic inference algorithm to create a unique prediction of labels required for evaluation. Recall that the reverse diffusion process of DPM can produce a diverse set of predictions, but the classification problem needs a single best guess.

To this end, when evaluating our DPM-GSP, we set $\mathbf{y}^{(T)}$ to be a zero vector $\mathbf{0}$, which is the average of $p(\mathbf{y}^{(T)}) = \mathcal{N}(\mathbf{y}^{(T)}; \mathbf{0}, \mathbf{I})$. Then for $t = T, \dots, 1$, the reverse diffusion process deterministically reconstructs $\mathbf{y}^{(t-1)}$ from $\mathbf{y}^{(t)}$ as the average of $p_\theta(\mathbf{y}^{(t-1)} | \mathbf{y}^{(t)})$. If the target is one-hot relaxation of discrete labels, we discretize the final prediction by choosing a dimension with maximum value.⁵

²One can easily extend DPM-GSP to learn on graphs associated with edge-wise attributes and targets (see Appendix C.3).

³We also compare with other diffusion strategies in Table 5.

⁴We highlight this point in Figure 4.

⁵We verify that our deterministic inference strategy indeed improves over the typical stochastic inference strategy in Figure 7.

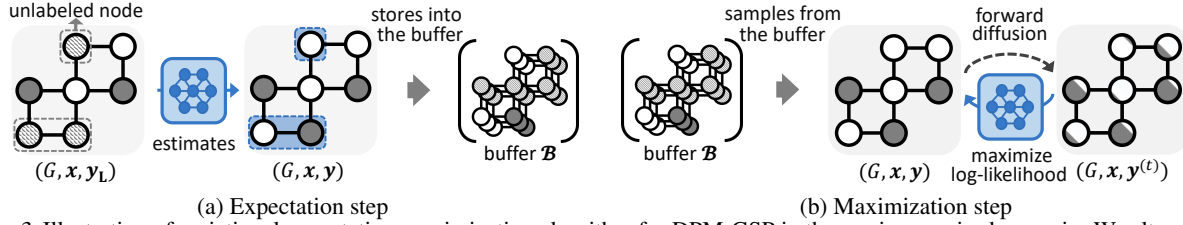


Figure 3. Illustration of variational expectation-maximization algorithm for DPM-GSP in the semi-supervised scenario. We alternatively (a) estimate the unlabeled nodes and (b) maximize log-likelihood using the estimated unlabeled nodes.

Algorithm 1 Semi-supervised training of DPM-GSP

- 1: **Input:** Graph G , attributes \mathbf{x} , and targets \mathbf{y}_L .
- 2: Train a mean-field GNN $p_\phi(\mathbf{y}|\mathbf{x}, G)$ on \mathbf{y}_L and G .
- 3: Initialize the buffer \mathcal{B} with samples from $p_\phi(\mathbf{y}_U|\mathbf{x}, G)$.
- 4: **repeat**
- 5: **for** $i = 1, \dots, N_1$ **do** ▷ Expectation step
- 6: Get $\mathbf{y}_U \sim p_\theta(\mathbf{y}_U|\mathbf{y}_L, \mathbf{x}, G)$ using manifold-constrained sampling. ▷ Appendix B
- 7: Update $\mathcal{B} \leftarrow \mathcal{B} \cup \{\mathbf{y}_U\}$.
- 8: If $|\mathcal{B}| > K$, remove oldest entity from \mathcal{B} .
- 9: **end for**
- 10: **for** $i = 1, \dots, N_2$ **do** ▷ Maximization step
- 11: Sample $\mathbf{y}_U \sim \mathcal{B}$.
- 12: Update θ to minimize \mathcal{L} in Equation (1) with G , \mathbf{x} , and $\mathbf{y} = \mathbf{y}_L \cup \mathbf{y}_U$.
- 13: **end for**
- 14: **until** converged

3.2. Semi-supervised node classification

In the semi-supervised setting, we consider training on a graph G with attributes \mathbf{x} where the targets \mathbf{y} are partially labeled. We denote the labeled and the unlabeled targets by \mathbf{y}_L and \mathbf{y}_U , respectively. To this end, we train a model to maximize the marginal log-likelihood $\log p_\theta(\mathbf{y}_L|G, \mathbf{x}) = \log \sum_{\mathbf{y}_U} p_\theta(\mathbf{y}_L, \mathbf{y}_U|G, \mathbf{x})$. However, since the marginalization over \mathbf{y}_U is intractable, we apply the variational expectation-maximization (Dempster et al., 1977; Wainwright et al., 2008, EM) algorithm to maximize a variational lower bound:

$$\log p_\theta(\mathbf{y}_L) \geq \mathbb{E}_{q_*(\mathbf{y}_U)}[\log p_\theta(\mathbf{y}_L, \mathbf{y}_U) - \log q_*(\mathbf{y}_U)],$$

where q_* is a variational distribution and the equality holds when $q_*(\mathbf{y}_U) = p_\theta(\mathbf{y}_U|\mathbf{y}_L)$. We omit the dependency of probabilities on a graph G and attributes \mathbf{x} for simplicity.

The variational EM algorithm maximizes the lower bound by iterating between an ‘‘expectation’’ step and a ‘‘maximization’’ step. The expectation step updates the variational distribution q_* to tighten the lower bound, i.e., update $q_*(\mathbf{y}_U)$ to match the true distribution $p_\theta(\mathbf{y}_U|\mathbf{y}_L)$. Then, the maximization step trains the distribution p_θ to maximize the lower bound using the current q_* . We describe the overall procedure in Algorithm 1.

Expectation step. In the expectation step, we update the

variational distribution $q_*(\mathbf{y}_U)$ to match the distribution of unobserved targets, i.e., $q_*(\mathbf{y}_U) = p_\theta(\mathbf{y}_U|\mathbf{y}_L)$. To this end, we introduce a buffer \mathcal{B} to store the last K samples from $p_\theta(\mathbf{y}_U|\mathbf{y}_L)$ and set $q_*(\mathbf{y}_U)$ as the empirical distribution of the buffer. Then one can infer that $q_*(\mathbf{y}_U) \approx p_\theta(\mathbf{y}_U|\mathbf{y}_L)$ if the buffer is sufficiently large and the parameter θ does not change much after each training step.

However, sampling from $p_\theta(\mathbf{y}_U|\mathbf{y}_L)$ is non-trivial since the reverse diffusion process of DPM only allows unconditional prediction $p_\theta(\mathbf{y})$. To this end, we apply manifold-constrained sampling (Chung et al., 2022), which constrains the reverse diffusion process to obtain a sample $\mathbf{y} \sim p_\theta(\mathbf{y})$ with maintaining the ground truth labels for \mathbf{y}_L . We describe the detailed sampling procedure in Appendix B.

We empirically observe a performance improvement from initializing the variational distribution $q_*(\mathbf{y}_U)$ as a good approximation to the true node label distribution $p(\mathbf{y}_U|\mathbf{y}_L)$. To this end, we initialize the buffer \mathcal{B} using samples from a pre-trained ‘‘mean-field’’ GNN $p_\phi(\mathbf{y}|\mathbf{x}, G)$ which outputs an independent joint distribution over node-wise labels, i.e., $p_\phi(\mathbf{y}|\mathbf{x}, G) = \prod_{i \in \mathcal{V}} p_\phi(y_i|\mathbf{x}, G)$.

Maximization step. In the maximization step, we update the distribution $p_\theta(\mathbf{y})$ to maximize the lower bound with respect to the current variational distribution $q_*(\mathbf{y}_U)$, i.e., samples from the buffer \mathcal{B} . This is equivalent to minimizing Equation (1) with targets \mathbf{y} set to the union of true targets \mathbf{y}_L and predicted targets $\mathbf{y}_U \sim \mathcal{B}$, i.e., $\mathbf{y} = \mathbf{y}_L \cup \mathbf{y}_U$.

4. Experiments

4.1. Inductive node classification

We first evaluate our DPM-GSP in an inductive setting. Here, we consider training a model on a set of fully labeled graphs and then testing the model on unseen graphs. As the backbone of DPM-GSP, we consider graph convolutional neural network (Kipf & Welling, 2016a, GCN), graph sample and aggregation (Hamilton et al., 2017, GraphSAGE), and graph attention network (Veličković et al., 2017, GAT).

Baselines. We compare DPM-GSP with a base GNN that we train to make unstructured prediction $p_\theta(\mathbf{y}|G, \mathbf{x}) = \prod_{i \in \mathcal{V}} p_\theta(y_i|G, \mathbf{x})$. We also compare with the recent GNN-based graph-structured prediction algorithms: graph Markov

Table 1. The inductive node classification accuracy. N-Acc and G-Acc denote the node-level and graph-level accuracy, respectively. **Bold** numbers indicate the best performance among the graph-structured prediction methods using the same GNN. Underlined numbers indicate the best performance. [†]We use the numbers reported by [Qu et al. \(2022\)](#).

Method	Pubmed		Cora		Citeseer	
	N-Acc	G-Acc	N-Acc	G-Acc	N-Acc	G-Acc
GMNN [†]	78.00 ±1.04	51.70 ±1.23	79.90 ±0.93	54.30 ±1.15	72.18 ±0.48	48.46 ±1.06
GCN	78.52 ±0.72	51.04 ±0.46	81.06 ±0.64	56.62 ±0.74	72.96 ±0.72	47.62 ±0.58
+SPN	79.20 ±0.52	52.90 ±0.41	82.23 ±0.48	59.16 ±0.30	73.96 ±0.84	48.66 ±1.04
+CLGNN	79.22 ±0.46	52.64 ±0.68	82.09 ±0.43	58.15 ±0.58	74.00 ±0.76	48.24 ±0.88
+DPM-GSP	80.01 ±0.47	54.49 ±0.33	83.90 ±0.69	59.72 ±0.66	74.96 ±0.89	49.86 ±0.85
GraphSAGE	77.42 ±0.32	49.24 ±1.36	81.68 ±0.22	58.15 ±0.66	73.59 ±0.72	45.12 ±0.94
+SPN	78.21 ±0.65	52.68 ±1.01	81.88 ±0.70	58.85 ±0.65	74.18 ±1.36	45.98 ±1.22
+CLGNN	77.97 ±1.24	51.26 ±2.71	82.28 ±0.44	59.56 ±1.27	74.57 ±0.44	46.69 ±1.13
+DPM-GSP	78.91 ±0.68	53.07 ±0.65	83.23 ±0.37	60.04 ±0.97	76.33 ±0.87	50.33 ±1.10
GAT	78.56 ±0.42	51.68 ±0.62	81.78 ±0.88	55.98 ±1.32	74.16 ±0.18	47.86 ±0.34
+SPN	79.16 ±0.21	52.65 ±0.66	83.42 ±0.52	58.51 ±0.64	74.78 ±0.66	48.76 ±0.87
+CLGNN	78.88 ±0.36	53.16 ±0.70	83.18 ±0.38	56.92 ±0.90	74.59 ±0.36	48.64 ±0.69
+DPM-GSP	79.89 ±0.26	54.60 ±0.48	84.36 ±0.59	60.15 ±0.51	76.20 ±0.65	52.03 ±0.90

Table 2. The inductive node classification performance. **Bold** numbers indicate the best performance among the graph-structured prediction methods using the same GNN. Underlined numbers indicate the best performance. [†]We use the numbers reported by [Qu et al. \(2022\)](#).

Method	DBLP	PPI-1		PPI-2		PPI-10		PPI-20	
	N-Acc	N-Acc	F1	N-Acc	F1	N-Acc	F1	N-Acc	F1
GMNN [†]	76.54 ±2.93	77.55 ±0.53	57.20 ±2.63	81.21 ±0.87	67.46 ±2.92	94.67 ±2.77	90.72 ±5.28	97.00 ±2.98	94.69 ±5.60
GCN	77.20 ±3.42	79.61 ±0.24	63.92 ±0.29	83.96 ±0.16	73.47 ±0.46	97.21 ±0.13	95.24 ±0.23	99.24 ±0.00	98.34 ±0.01
+SPN [†]	79.50 ±0.10	77.07 ±0.05	54.15 ±0.17	78.02 ±0.05	55.73 ±0.15	80.59 ±0.04	61.36 ±0.11	82.56 ±0.20	66.70 ±0.77
+CLGNN	81.41 ±1.17	80.09 ±0.33	64.76 ±0.20	84.20 ±0.12	73.34 ±0.64	97.45 ±0.10	95.64 ±0.20	99.31 ±0.01	98.66 ±0.01
+DPM-GSP	83.93 ±1.07	83.00 ±0.30	71.20 ±0.38	87.24 ±0.24	77.35 ±0.45	98.17 ±0.08	96.87 ±0.15	99.45 ±0.02	99.10 ±0.02
GraphSAGE	75.24 ±3.26	80.04 ±0.07	66.83 ±0.37	83.65 ±0.35	73.21 ±0.26	97.67 ±0.05	96.05 ±0.09	99.47 ±0.02	99.10 ±0.02
+SPN [†]	78.86 ±3.70	82.11 ±0.03	68.56 ±0.07	85.40 ±0.05	74.45 ±0.07	95.28 ±0.02	91.99 ±0.04	98.55 ±0.02	97.56 ±0.03
+CLGNN	76.43 ±2.43	81.50 ±0.11	67.74 ±0.22	84.05 ±0.40	73.74 ±0.38	97.68 ±0.03	96.08 ±0.04	99.49 ±0.02	99.14 ±0.04
+DPM-GSP	81.04 ±2.57	83.50 ±0.27	72.09 ±0.22	87.80 ±0.11	78.88 ±0.23	98.27 ±0.07	97.05 ±0.09	99.60 ±0.03	99.31 ±0.04
GAT	78.64 ±3.12	77.87 ±0.94	63.64 ±0.25	81.70 ±0.58	69.86 ±0.87	97.18 ±0.23	95.19 ±0.41	99.45 ±0.01	99.07 ±0.03
+SPN [†]	84.84 ±0.73	78.13 ±0.21	62.25 ±0.32	83.55 ±0.12	72.37 ±0.18	96.68 ±0.13	94.41 ±0.21	99.04 ±0.06	98.38 ±0.10
+CLGNN	82.79 ±1.45	79.01 ±0.17	64.02 ±0.40	82.78 ±0.18	70.39 ±0.79	97.24 ±0.24	95.26 ±0.04	99.46 ±0.02	99.09 ±0.03
+DPM-GSP	83.89 ±2.53	81.68 ±0.73	69.89 ±0.49	86.21 ±0.20	75.58 ±0.23	98.24 ±0.08	97.00 ±0.15	99.62 ±0.01	99.34 ±0.02

neural network ([Qu et al., 2019](#), GMNN), structured proxy network ([Qu et al., 2022](#), SPN), and collective learning graph neural network ([Hang et al., 2021](#), CLGNN). We describe the hyper-parameter settings in [Appendix C.1](#).

Datasets. We follow [Qu et al. \(2022\)](#) and experiment on both small-scale and large-scale graphs. We construct small-scale graphs from Cora, Citeseer, and Pubmed ([Yang et al., 2016](#)). We also construct large-scale graphs from PPI ([Zitnik & Leskovec, 2017](#)) and DBLP datasets ([Tang et al., 2008](#)). In addition, to make the task challenging, we consider limiting the number of training graphs in the PPI dataset. We let PPI- k denote a dataset with k graphs for training.

Evaluation metrics. For all datasets, we evaluate node-level accuracy, i.e., the ratio of nodes associated with a correct prediction. For small-scale graphs, i.e., Pubmed, Cora, and Citeseer, we also report the graph-level accuracy,

which measures the ratio of graphs where all the node-wise predictions are correct. For the PPI datasets, we also report the micro-F1 score that is robust against the imbalance in the distribution of labels. We report the performance measured using ten and five different random seeds for small-scale and large-scale graphs, respectively.

Results. We report the results in [Table 1](#) and [Table 2](#) for small-scale and large-scale graphs, respectively. Here, one may observe that our DPM-GSP provides consistent gains to the GNNs that make unstructured predictions. Furthermore, our DPM-GSP outperforms all the baselines consistently except for DBLP. Our algorithm also achieves the best score for graph-level accuracy, which highlights the ability of our algorithm to incorporate structure into the prediction.

Table 3. The transductive node classification accuracy. **Bold** numbers indicate the best performance among the graph-structured prediction methods using the same GNN. Underlined numbers indicate the best performance. ^{†‡*}We use the numbers reported by Bo et al. (2022), Ma et al. (2019b), and Wang et al. (2021) respectively.

Method	Pubmed	Cora	Citeseer	Photo	Computer	Cornell	Wisconsin	Texas
LP [†]	70.4 ±0.00	50.6 ±0.00	71.8 ±0.00	79.8 ±3.40	79.0 ±4.80	-	-	-
GLP [†]	78.8 ±0.40	80.3 ±0.20	71.7 ±0.60	89.6 ±0.70	81.9 ±1.10	-	-	-
PTA [†]	80.1 ±0.10	83.0 ±0.50	71.6 ±0.40	90.7 ±2.10	82.3 ±0.90	-	-	-
LCM*	77.7 ±1.90	83.3 ±0.70	72.2 ±0.50	-	-	-	-	-
GMNN	81.7 ±0.56	83.8 ±0.86	73.0 ±0.72	91.3 ±1.56	82.8 ±1.52	53.5 ±7.02	61.8 ±8.24	68.1 ±7.72
GCN	78.6 ±0.52	81.5 ±0.68	71.6 ±0.72	90.4 ±0.70	82.3 ±1.51	57.6 ±6.12	58.7 ±5.58	57.2 ±6.01
+ G3NN-LSM [‡]	77.9 ±0.40	82.5 ±0.20	74.4 ±0.30	-	-	-	-	-
+ G3NN-SBM [‡]	78.4 ±0.60	82.2 ±0.20	74.5 ±0.40	-	-	-	-	-
+ CLGNN	80.2 ±0.49	81.6 ±0.32	71.4 ±0.68	90.8 ±1.11	82.9 ±1.75	55.6 ±7.06	62.3 ±2.74	65.9 ±5.43
+ DPM-GSP	82.6 ±0.90	82.9 ±0.41	74.0 ±0.62	91.5 ±1.01	83.4 ±1.88	63.6 ±5.72	67.5 ±2.76	68.4 ±3.19
GraphSAGE	77.2 ±0.88	80.0 ±0.87	71.2 ±0.66	91.0 ±0.84	82.1 ±0.97	74.3 ±2.16	81.1 ±5.56	82.1 ±5.43
+ CLGNN	77.4 ±0.47	81.0 ±0.56	71.9 ±0.82	91.2 ±0.83	83.1 ±1.78	74.0 ±2.75	83.1 ±3.94	81.6 ±6.59
+ DPM-GSP	78.4 ±1.38	83.2 ±0.43	72.6 ±0.96	91.9 ±1.16	84.0 ±1.43	75.1 ±2.91	84.1 ±3.44	83.0 ±4.68
GAT	79.1 ±0.36	82.4 ±0.66	72.1 ±0.68	90.6 ±1.11	83.3 ±1.53	58.6 ±4.26	57.8 ±6.71	58.1 ±3.48
+ G3NN-LSM [‡]	77.6 ±0.70	82.9 ±0.30	73.1 ±0.50	-	-	-	-	-
+ G3NN-SBM [‡]	77.4 ±0.40	82.9 ±0.30	74.0 ±0.30	-	-	-	-	-
+ CLGNN	80.8 ±0.42	83.3 ±0.51	73.2 ±0.66	90.9 ±1.15	83.6 ±1.38	57.3 ±4.32	65.7 ±3.64	61.9 ±6.33
+ DPM-GSP	82.0 ±0.29	84.2 ±0.70	74.6 ±0.62	92.2 ±1.05	85.2 ±1.31	63.0 ±5.27	67.1 ±4.36	64.0 ±5.58

4.2. Transductive node classification

Next, we evaluate the performance of our algorithm for transductive node classification. We apply Algorithm 1 to train our DPM-GSP in this setting.

Baselines. We first compare our method with label propagation (Wang & Zhang, 2006, LP), and LP-based methods such as generalized label propagation (Li et al., 2019, GLP), and propagation then training adaptively (Dong et al., 2021, PTA). Then we consider learning the coupling matrix (Wang et al., 2021, LCM), which is a CRF-based method. We also compare with base GNN, GMNN, and CLGNN, introduced in Section 4.1. Finally, we also compare with generative graph models with graph neural networks (Ma et al., 2019b, G3NN). We describe the hyper-parameter settings in Appendix C.2.

Datasets. We use eight datasets: Pubmed, Cora, Citeseer, Amazon Photo and Computer (Shchur et al., 2018), Cornell, Wisconsin, and Texas (Pei et al., 2019). The data partition criterion used for Pubmed, Cora, and Citeseer is the same as in Yang et al. (2016), where 20 nodes per class are used for training. For Photo and Computer, the criterion is the same as in Shchur et al. (2018), where 20 nodes per class are used for training. For Cornell, Wisconsin, and Texas, the criterion is the same as in Zhu et al. (2020), where 48% of nodes are used for training. We report the accuracy measured using ten random seeds for all datasets.

Results. We report the results in Table 3. One can again observe how our algorithm consistently improves the base GNNs. Furthermore, our outperforms all the existing al-

gorithms, even when sharing the GNN backbone with some structured prediction algorithms. Along with the experiments for inductive node classification, these results highlight the superiority of DPM-GSP in making graph-structured predictions.

4.3. Algorithmic reasoning

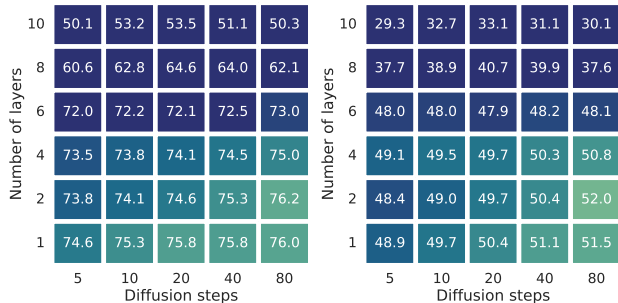
We also evaluate our DPM-GSP to predict the outcomes of graph algorithms, e.g., computing the shortest between two nodes. Solving such a task using GNNs has gained much attention since it builds connections between deep learning and classical computer science algorithms. To this end, researchers have developed tailored algorithms like iterative energy minimization (Du et al., 2022, IREM) and PonderNet (Banino et al., 2021). Here, we show that the capability of DPM-GSP to make a structured prediction even allows good reasoning ability.

We evaluate the performance of our DPM-GSP on three graph algorithmic reasoning benchmarks: edge copy, shortest path, and connected component, proposed by Du et al. (2022). The edge copy task aims to replicate the edge attributes in the output. The shortest path task computes the shortest path between all pairs of nodes. The connected component task identifies which nodes belong to the same connected component. As these tasks are defined on edge-wise targets, we modify DPM-GSP to make edge-wise predictions. The detailed diffusion scheme and the GNN architectures are described in Appendix C.3.

Datasets. Following Du et al. (2022), we use a training dataset composed of graphs of varying sizes, ranging from

Table 4. Performance on graph algorithmic reasoning tasks. **Bold** numbers indicate the best performance for each task. The same size and large size indicate the performance on graphs with ten and 15 nodes, respectively. †We use the numbers reported by Du et al. (2022).

Method	Edge copy		Connected components		Shortest path	
	Same size	Large size	Same size	Large size	Same size	Large size
Feedforward†	0.3016	0.3124	0.1796	0.3460	0.1233	1.4089
Recurrent†	0.3015	0.3113	0.1794	0.2766	0.1259	0.1083
Programmatic†	0.3053	0.4409	0.2338	3.1381	0.1375	0.1375
Iterative feedforward†	0.6163	0.6163	0.4908	0.4908	0.4908	0.7688
IREM†	0.0019	0.0019	0.1424	0.2171	0.0274	0.0464
DPM-GSP	0.0011	0.0038	0.0724	0.1884	0.0138	0.0286



(a) Node-level accuracy (b) Graph-level accuracy

Figure 4. Performance with varying number of GNN layers and number of diffusion steps. Increasing the number of GNN layers alone does not lead to improved accuracy, but increasing the number of diffusion steps results in better accuracy.

two to ten nodes. Then, we evaluate performance on graphs with ten nodes. Furthermore, we also use graphs with 15 nodes to evaluate generalization capabilities. We report the performance using element-wise mean square error.

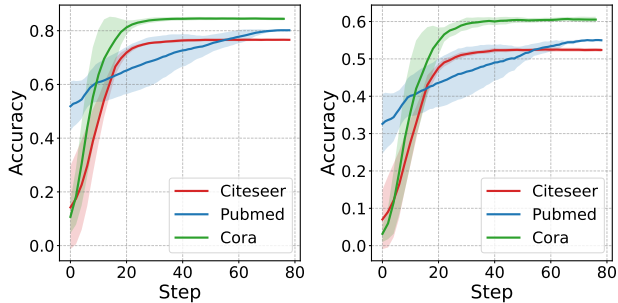
Baselines. We compare our method with five methods reported by Du et al. (2022), including a feedforward neural network, recurrent neural network, Pondernet, iterative feedforward, and IREM.

Results. We report the results in Table 4. Our DPM-GSP outperforms the considered baselines for five out of the six tasks. In particular, DPM-GSP significantly improves all the baselines for shortest path and connected components tasks. These results suggest that the diffusion model can easily solve algorithmic reasoning tasks thanks to its superior ability to make structured predictions.

4.4. Ablation studies

Here, we conduct ablation studies to analyze our framework. All the results are averaged over ten different random seeds.

Number of GNN layers vs. diffusion steps. We first verify that our DPM-GSP method does not solely rely on increasing the number of GNN layers to improve node classification performance. To this end, we measure performance by varying the number of GNN layers and the number of diffusion steps. We report the corresponding results in the Figure 4.



(a) Node-level accuracy (b) Graph-level accuracy

Figure 5. Intermediate accuracy with steps in the reverse diffusion process. The solid line and shaded region represent the mean and standard deviation of the accuracy, respectively. The iteration in the reverse diffusion process gradually increases accuracy.

One can observe that just increasing the number of GNN layers does not improve performance, whereas increasing the number of diffusion steps results in better performance.

Accuracy over diffusion steps. We investigate whether the iteration in the reverse diffusion process progressively improves the quality of predictions. In Figure 5, we plot the changes in node-level and graph-level accuracy in the reverse diffusion process as the number of iterations increases. The results confirm that the iterative inference process gradually increases accuracy, eventually reaching convergence.

Deterministic vs. stochastic inference. We compare the original stochastic reverse diffusion process with our deterministic inference. In Figure 6, we plot the changes in accuracy for various temperatures λ , where the reverse diffusion process uses $\lambda^2 \sigma_t^2$ as the variance for each step $t = 1, \dots, T$. Note that setting $\lambda = 0$ reduces the stochastic inference scheme to our deterministic one. One can see that reducing the randomness of DPM gives a better prediction.

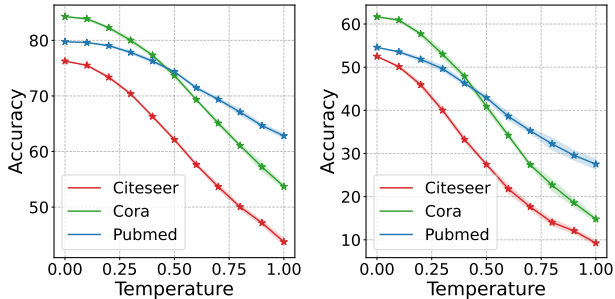
We also consider sampling various numbers of predictions for node-wise aggregation to improve performance. In Figure 7, when the sample size is increased to 1000, the deterministic and the stochastic inference schemes show similar node-level accuracy, whereas deterministic inference still yields a higher graph-level accuracy. This is because node-wise aggregation ignores the graph structure by aggregating the labels independently for each node.

Table 5. The inductive node classification accuracy. N-Acc and G-Acc denote the node-level and graph-level accuracy, respectively. The backbone network is GAT. The Gaussian diffusion process outperforms the considered baselines specialized to discrete label.

Method	Pubmed		Cora		Citeseer	
	N-Acc	G-Acc	N-Acc	G-Acc	N-Acc	G-Acc
Absorbing	79.08 ±0.86	53.45 ±0.48	81.66 ±1.40	55.34 ±1.49	74.22 ±0.84	49.37 ±1.11
Uniform	70.78 ±0.89	38.79 ±1.16	63.26 ±0.82	25.88 ±1.08	57.05 ±0.61	22.51 ±1.22
Bit-upscale	79.42 ±0.79	53.92 ±0.27	82.62 ±0.32	56.25 ±0.42	75.51 ±0.58	51.19 ±0.80
Gaussian	79.89 ±0.26	54.60 ±0.48	84.36 ±0.59	60.15 ±0.51	76.20 ±0.65	52.03 ±0.90

Table 6. The inductive node classification accuracy and inference time (ms). N-Acc and G-Acc denote the node-level and graph-level accuracy, respectively. The backbone network is GCN. We let SPN (T) and DPM-GSP (T) denote the algorithms with T belief propagation steps and T diffusion steps, respectively. DPM-GSP shows a competitive trade-off between running time and accuracy.

Methods	Pubmed			Cora			Citeseer		
	N-Acc	G-Acc	Time	N-Acc	G-Acc	Time	N-Acc	G-Acc	Time
SPN (20)	79.12 ±0.60	52.88 ±0.44	4.85	82.23 ±0.48	59.16 ±0.30	4.95	73.96 ±0.84	48.66 ±1.04	4.52
SPN (100)	79.20 ±0.52	52.90 ±0.41	18.3	82.18 ±0.50	59.14 ±0.34	19.8	73.98 ±0.76	48.65 ±0.94	17.6
CLGNN	79.22 ±0.46	52.64 ±0.68	24.8	82.09 ±0.43	58.15 ±0.58	25.6	74.06 ±0.72	48.24 ±0.88	23.2
DPM-GSP (3)	79.19 ±0.69	52.27 ±1.01	5.05	83.06 ±0.56	59.19 ±0.78	5.58	74.12 ±0.69	48.60 ±0.88	5.21
DPM-GSP (80)	80.01 ±0.47	54.49 ±0.33	123.	83.90 ±0.69	59.72 ±0.66	129.	74.96 ±0.89	49.86 ±0.85	120.



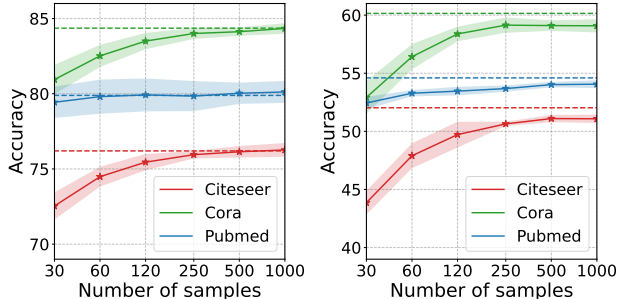
(a) Node-level accuracy (b) Graph-level accuracy

Figure 6. Accuracy with varying temperature of stochastic prediction. The solid line and shaded regions represent the mean and standard deviation of the accuracy, respectively. Reducing the randomness of DPM increases the accuracy.

Gaussian vs. discrete diffusion. We validate our Gaussian diffusion process that relaxes the discrete label space by comparing with diffusion processes explicitly designed for discrete target space. We compare with absorbing and uniform transition proposed by Austin et al. (2021). We also adapt the bit upscaling transition proposed by Hooeboom et al. (2022a) to our setting.

We report the results in Table 5. Surprisingly, one can observe that the Gaussian diffusion process outperforms the considered baselines. We hypothesize that continuous relaxation allows better propagation of “uncertainty” in predictions, similar to how algorithm-like belief propagation (Murphy et al., 2013) works. We leave the investigation of a diffusion process specialized to our setting for future work.

Running time vs. performance. Finally, we investigate whether the DPM-GSP can make a good trade-off between running time and performance. In Table 6, we report the performances of DPM-GSP with varying numbers of diffusion steps and running times. One can observe that our



(a) Node-level accuracy (b) Graph-level accuracy

Figure 7. Accuracy with varying number of samples for stochastic inference. The solid line and shaded regions represent the mean and standard deviation of the accuracy, respectively. The dashed line represents the accuracy of deterministic inference scheme. Deterministic inference performs at least as well as stochastic inference for the considered number of samples.

DPM-GSP with only three diffusion steps shows competitive performances compared to the SPN and CLGNN while running in similar or less time. Also, while increasing the inference times of the SPN does not enhance performance, DPM-GSP shows further performance improvement.

5. Conclusion

We propose diffusion probabilistic models for solving graph-structured prediction (DPM-GSP) in both fully supervised and semi-supervised settings. Extensive experiments show that DPM-GSP outperforms existing methods. We believe accelerating our framework with faster diffusion-based models, e.g., denoising diffusion implicit models (Song et al., DDIM), or combining with other diffusion schemes, e.g., simplex diffusion (Richemond et al., 2022), are important future research directions.

References

- Austin, J., Johnson, D. D., Ho, J., Tarlow, D., and van den Berg, R. Structured denoising diffusion models in discrete state-spaces. *Advances in Neural Information Processing Systems*, 34:17981–17993, 2021. 8
- Banino, A., Balaguer, J., and Blundell, C. PonderNet: Learning to ponder. In *8th ICML Workshop on Automated Machine Learning (AutoML)*, 2021. 6
- Belanger, D. and McCallum, A. Structured prediction energy networks. In *International Conference on Machine Learning*, pp. 983–992. PMLR, 2016. 2
- Besag, J. Statistical analysis of non-lattice data. *Journal of the Royal Statistical Society: Series D (The Statistician)*, 24(3):179–195, 1975. 2
- Bo, D., Hu, B., Wang, X., Zhang, Z., Shi, C., and Zhou, J. Regularizing graph neural networks via consistency-diversity graph augmentations. *Proceedings of the AAAI Conference on Artificial Intelligence*, 36(4):3913–3921, Jun. 2022. 6, 16
- Chakrabarti, S., Dom, B., and Indyk, P. Enhanced hypertext categorization using hyperlinks. *Acm Sigmod Record*, 27(2):307–318, 1998. 1
- Chamberlain, B., Rowbottom, J., Gorinova, M. I., Bronstein, M., Webb, S., and Rossi, E. Grand: Graph neural diffusion. In *International Conference on Machine Learning*, pp. 1407–1418. PMLR, 2021. 2
- Chen, S., Sun, P., Song, Y., and Luo, P. Diffusiondet: Diffusion model for object detection. *arXiv preprint arXiv:2211.09788*, 2022a. 2
- Chen, T., Li, L., Saxena, S., Hinton, G., and Fleet, D. J. A generalist framework for panoptic segmentation of images and videos. *arXiv preprint arXiv:2210.06366*, 2022b. 2
- Chung, H., Sim, B., Ryu, D., and Ye, J. C. Improving diffusion models for inverse problems using manifold constraints. *arXiv preprint arXiv:2206.00941*, 2022. 2, 4, 13
- Clevert, D.-A., Unterthiner, T., and Hochreiter, S. Fast and accurate deep network learning by exponential linear units (elus). *arXiv preprint arXiv:1511.07289*, 2015. 14, 15, 16, 17
- Dempster, A. P., Laird, N. M., and Rubin, D. B. Maximum likelihood from incomplete data via the em algorithm. *Journal of the Royal Statistical Society: Series B (Methodological)*, 39(1):1–22, 1977. 4
- Dhariwal, P. and Nichol, A. Diffusion models beat gans on image synthesis. *Advances in Neural Information Processing Systems*, 34:8780–8794, 2021. 2
- Dong, H., Chen, J., Feng, F., He, X., Bi, S., Ding, Z., and Cui, P. On the equivalence of decoupled graph convolution network and label propagation. In *Proceedings of the Web Conference 2021*, pp. 3651–3662, 2021. 6
- Du, Y., Li, S., Tenenbaum, J., and Mordatch, I. Learning iterative reasoning through energy minimization. In *International Conference on Machine Learning*, pp. 5570–5582. PMLR, 2022. 2, 6, 7, 17
- Garcia Satorras, V., Akata, Z., and Welling, M. Combining generative and discriminative models for hybrid inference. *Advances in Neural Information Processing Systems*, 32, 2019. 2
- Graber, C. and Schwing, A. Graph structured prediction energy networks. *Advances in Neural Information Processing Systems*, 32, 2019. 1
- Graber, C., Meshi, O., and Schwing, A. Deep structured prediction with nonlinear output transformations. *Advances in Neural Information Processing Systems*, 31, 2018. 2
- Hamilton, W., Ying, Z., and Leskovec, J. Inductive representation learning on large graphs. *NeurIPS*, 30, 2017. 2, 4
- Hang, M., Neville, J., and Ribeiro, B. A collective learning framework to boost gnn expressiveness for node classification. In *International Conference on Machine Learning*, pp. 4040–4050. PMLR, 2021. 1, 2, 5
- Ho, J., Jain, A., and Abbeel, P. Denoising diffusion probabilistic models. *Advances in Neural Information Processing Systems*, 2020. 1, 3, 12
- Hoogeboom, E., Gritsenko, A. A., Bastings, J., Poole, B., van den Berg, R., and Salimans, T. Autoregressive diffusion models. In *International Conference on Learning Representations*, 2022a. URL <https://openreview.net/forum?id=Lm8T39vLDTE>. 8
- Hoogeboom, E., Satorras, V. G., Vignac, C., and Welling, M. Equivariant diffusion for molecule generation in 3d. In *International Conference on Machine Learning*, pp. 8867–8887. PMLR, 2022b. 2
- Hu, W., Liu, B., Gomes, J., Zitnik, M., Liang, P., Pande, V., and Leskovec, J. Strategies for pre-training graph neural networks. In *International Conference on Learning Representations (ICLR)*, 2020. 17
- Kingma, D. P. and Ba, J. Adam: A method for stochastic optimization. *arXiv preprint arXiv:1412.6980*, 2014. 14, 15, 16, 17

- Kipf, T. N. and Welling, M. Semi-supervised classification with graph convolutional networks. *arXiv preprint arXiv:1609.02907*, 2016a. 1, 2, 4
- Kipf, T. N. and Welling, M. Variational graph auto-encoders. *arXiv preprint arXiv:1611.07308*, 2016b. 2
- Lafferty, J., McCallum, A., and Pereira, F. C. Conditional random fields: Probabilistic models for segmenting and labeling sequence data. 2001. 1
- Li, Q., Wu, X.-M., Liu, H., Zhang, X., and Guan, Z. Label efficient semi-supervised learning via graph filtering. In *Proceedings of the IEEE/CVF Conference on Computer Vision and Pattern Recognition*, pp. 9582–9591, 2019. 6
- Li, X. L., Thickstun, J., Gulrajani, I., Liang, P., and Hashimoto, T. B. Diffusion-LM improves controllable text generation. *arXiv preprint arXiv:2205.14217*, 2022. 2
- Ma, J., Tang, W., Zhu, J., and Mei, Q. A flexible generative framework for graph-based semi-supervised learning. *Advances in Neural Information Processing Systems*, 32, 2019a. 2, 16
- Ma, T., Xiao, C., Shang, J., and Sun, J. CGNF: Conditional graph neural fields, 2019b. URL <https://openreview.net/forum?id=ryxMX2R9YQ>. 1, 6
- Murphy, K., Weiss, Y., and Jordan, M. I. Loopy belief propagation for approximate inference: An empirical study. *arXiv preprint arXiv:1301.6725*, 2013. 8
- Nair, V. and Hinton, G. E. Rectified linear units improve restricted boltzmann machines. In *Proceedings of the 27th international conference on machine learning (ICML-10)*, pp. 807–814, 2010. 14, 15, 16
- Neville, J. and Jensen, D. Iterative classification in relational data. In *Proc. AAAI-2000 workshop on learning statistical models from relational data*, pp. 13–20, 2000. 2
- Nichol, A. Q. and Dhariwal, P. Improved denoising diffusion probabilistic models. In *International Conference on Machine Learning*, pp. 8162–8171. PMLR, 2021. 12
- Patil, N., Patil, A., and Pawar, B. Named entity recognition using conditional random fields. *Procedia Computer Science*, 167:1181–1188, 2020. 2
- Pei, H., Wei, B., Chang, K. C.-C., Lei, Y., and Yang, B. Geom-gcn: Geometric graph convolutional networks. In *International Conference on Learning Representations*, 2019. 6
- PVS, A. and Karthik, G. Part-of-speech tagging and chunking using conditional random fields and transformation based learning. *Shallow Parsing for South Asian Languages*, 21:21–24, 2007. 2
- Qu, M., Bengio, Y., and Tang, J. Gmnn: Graph markov neural networks. In *International conference on machine learning*, pp. 5241–5250. PMLR, 2019. 1, 2, 5, 15, 16
- Qu, M., Cai, H., and Tang, J. Neural structured prediction for inductive node classification. *arXiv preprint arXiv:2204.07524*, 2022. 1, 2, 5, 14, 15
- Richemond, P. H., Dieleman, S., and Doucet, A. Categorical sdes with simplex diffusion. *arXiv preprint arXiv:2210.14784*, 2022. 8
- Sen, P., Namata, G., Bilgic, M., Getoor, L., Galligher, B., and Eliassi-Rad, T. Collective classification in network data. *AI magazine*, 29(3):93–93, 2008. 1
- Shchur, O., Mumme, M., Bojchevski, A., and Günnemann, S. Pitfalls of graph neural network evaluation. *arXiv preprint arXiv:1811.05868*, 2018. 2, 6
- Sohl-Dickstein, J., Weiss, E., Maheswaranathan, N., and Ganguli, S. Deep unsupervised learning using nonequilibrium thermodynamics. In *International Conference on Machine Learning*, pp. 2256–2265. PMLR, 2015. 2
- Song, J., Meng, C., and Ermon, S. Denoising diffusion implicit models. In *International Conference on Learning Representations*. 8
- Sutton, C., McCallum, A., et al. An introduction to conditional random fields. *Foundations and Trends® in Machine Learning*, 4(4):267–373, 2012. 2
- Tang, J., Zhang, J., Yao, L., Li, J., Zhang, L., and Su, Z. Arnetminer: extraction and mining of academic social networks. In *Proceedings of the 14th ACM SIGKDD international conference on Knowledge discovery and data mining*, pp. 990–998, 2008. 2, 5
- Vaswani, A., Shazeer, N., Parmar, N., Uszkoreit, J., Jones, L., Gomez, A. N., Kaiser, Ł., and Polosukhin, I. Attention is all you need. *Advances in neural information processing systems*, 30, 2017. 12
- Veličković, P., Cucurull, G., Casanova, A., Romero, A., Lio, P., and Bengio, Y. Graph attention networks. *arXiv preprint arXiv:1710.10903*, 2017. 2, 4
- Wainwright, M. J., Jordan, M. I., et al. Graphical models, exponential families, and variational inference. *Foundations and Trends® in Machine Learning*, 1(1–2):1–305, 2008. 4

- Wang, B., Jia, J., and Gong, N. Z. Semi-supervised node classification on graphs: Markov random fields vs. graph neural networks. In *AAAI*, pp. 10093–10101, 2021. [6](#), [16](#)
- Wang, F. and Zhang, C. Label propagation through linear neighborhoods. In *Proceedings of the 23rd international conference on Machine learning*, pp. 985–992, 2006. [2](#), [6](#)
- Xu, K., Hu, W., Leskovec, J., and Jegelka, S. How powerful are graph neural networks? *arXiv preprint arXiv:1810.00826*, 2018. [1](#)
- Yang, Z., Cohen, W., and Salakhudinov, R. Revisiting semi-supervised learning with graph embeddings. In *International conference on machine learning*, pp. 40–48. PMLR, 2016. [2](#), [5](#), [6](#)
- Zhou, L., Du, Y., and Wu, J. 3d shape generation and completion through point-voxel diffusion. In *Proceedings of the IEEE/CVF International Conference on Computer Vision*, pp. 5826–5835, 2021. [2](#)
- Zhu, J., Yan, Y., Zhao, L., Heimann, M., Akoglu, L., and Koutra, D. Beyond homophily in graph neural networks: Current limitations and effective designs. *Advances in Neural Information Processing Systems*, 33:7793–7804, 2020. [2](#), [6](#)
- Zitnik, M. and Leskovec, J. Predicting multicellular function through multi-layer tissue networks. *Bioinformatics*, 33(14):i190–i198, 2017. [2](#), [5](#)

A. Detailed descriptions of DPM-GSP

In this section, we describe the detailed components of DPM-GSP.

Variiances schedule. To determine the variiances schedule β_1, \dots, β_T , we use the cosine beta schedule suggested by Nichol & Dhariwal (2021). Here, we set the offset parameter to 0.008.

Detailed reverse diffusion process. In Section 3.1, we parameterize probabilistic distribution of the reverse diffusion step $p_{\theta}(\mathbf{y}^{(t-1)}|\mathbf{y}^{(t)})$ as $\mathcal{N}(\mathbf{y}^{(t-1)}; \boldsymbol{\mu}_{\theta}(\mathbf{x}, \mathbf{y}^{(t)}, G, t), \sigma_t^2)$. Here, we set σ_t^2 to β_t . Following Ho et al. (2020), we also define $\mu_{\theta}(\mathbf{x}, \mathbf{y}^{(t)}, G, t)$ as follows:

$$\mu_{\theta}(\mathbf{x}, \mathbf{y}^{(t)}, G, t) = \frac{1}{\sqrt{\bar{\alpha}_t}} \left(\mathbf{y}^{(t)} - \frac{\beta_t}{\sqrt{1 - \bar{\alpha}_t}} \boldsymbol{\epsilon}_{\theta}(\mathbf{x}, \mathbf{y}^{(t)}, G, t) \right), \quad (2)$$

where $\bar{\alpha}_t$ is $\prod_{i=1}^t \alpha_i$. Here, parameterization of the residual function $\boldsymbol{\epsilon}_{\theta}(\mathbf{x}, \mathbf{y}^{(t)}, G, t)$ enables residual-matching training objective (Ho et al., 2020), which is further simplification of Equation (1). Specifically, we parameterize $\boldsymbol{\epsilon}_{\theta}(\mathbf{x}, \mathbf{y}^{(t)}, G, t)$ using a L -layer GNN as follows:

$$\begin{aligned} \boldsymbol{\epsilon}_{\theta}(\mathbf{x}, \mathbf{y}^{(t)}, G, t) &= g(h^{(L)}) \\ h_i^{(\ell)} &= (\text{COMBINE}^{(\ell)}(h_i^{(\ell-1)}, a_i^{(\ell)}) + f(t)) \| y_i^{(t)}, \\ a_i^{(\ell)} &= \text{AGGREGATE}^{(\ell)}(\{h_j^{(\ell-1)} | (i, j) \in \mathcal{E}\}), \end{aligned}$$

where $g(h^{(L)})$ is an MLP that estimates the residual using the final node representation. $\text{AGGREGATE}(\cdot)$ and $\text{COMBINE}(\cdot)$ functions are identical to the backbone GNN, and $\cdot \| \cdot$ indicates the concatenation. Here, h_i^0 is initialized by concatenating the node features and noisy label $x_i \| y_i^{(t)}$. The $f(\cdot)$ is a time embedding function that consists of a sinusoidal positional embedding function (Vaswani et al., 2017) and two-layer MLP. In this paper, we fix the dimension of sinusoidal positional embedding to 128.

Detailed training objective. In Section 3.1, we define the training objective of DPM-GSP in terms of estimated average $\boldsymbol{\mu}_{\theta}(\mathbf{x}, \mathbf{y}^{(t)}, G, t)$. Here, Equation (2) enables defining the further simplified objective as follows:

$$\mathcal{L} = \sum_{t=1}^T \mathbb{E}_{\boldsymbol{\epsilon} \sim \mathcal{N}(0, \mathbf{I})} \left[\frac{\beta_t^2}{2\sigma_t^2 \alpha_t (1 - \bar{\alpha}_t)} \left\| \boldsymbol{\epsilon} - \boldsymbol{\epsilon}_{\theta}(\mathbf{x}, \sqrt{\bar{\alpha}_t} \mathbf{y}^{(0)} + \sqrt{1 - \bar{\alpha}_t} \boldsymbol{\epsilon}, G, t) \right\|_2^2 \right]$$

where the detailed derivation follows Ho et al. (2020). An additional suggestion from Ho et al. (2020) is to set all weights of the mean squared error to one instead of $\frac{\beta_t^2}{2\sigma_t^2 \alpha_t (1 - \bar{\alpha}_t)}$. We employ this idea by introducing a hyper-parameter called ‘‘unweighted mean squared error’’, with a True value indicating that all weights of the mean square error are set to one.

B. Manifold-constrained sampling

To sample \mathbf{y}_U from $p_\theta(\mathbf{y}_U|\mathbf{y}_L)$, we introduce a manifold-constrained sampling method proposed by Chung et al. (2022). Here, the update rule of the reverse process for $t = 0, \dots, T - 1$ is modified as follows:

$$\begin{aligned}\mathbf{y}'^{(t)} &= \frac{1}{\sqrt{\alpha_t}} \left(\mathbf{y}^{(t+1)} - \frac{\beta_{t+1}}{\sqrt{1 - \bar{\alpha}_{t+1}}} \boldsymbol{\epsilon}_\theta(\mathbf{x}, \mathbf{y}^{(t+1)}, G, t + 1) \right) + \sigma_{t+1} \mathbf{z}, \quad \mathbf{z} \sim \mathcal{N}(\mathbf{z}; \mathbf{0}, \lambda^2 \mathbf{I}), \\ \mathbf{y}_U^{(t)} &= \bar{\mathbf{P}} \left(\mathbf{y}'^{(t)} - \gamma \frac{\partial}{\partial \mathbf{y}^{(t+1)}} \|\mathbf{y}_L - \mathbf{P} \hat{\mathbf{y}}\|_2^2 \right) \\ \mathbf{y}_L^{(t)} &= \sqrt{\bar{\alpha}_t} \mathbf{y}_L + \sqrt{1 - \bar{\alpha}_t} \mathbf{z}, \quad \mathbf{z} \sim \mathcal{N}(\mathbf{z}; \mathbf{0}, \lambda^2 \mathbf{I}).\end{aligned}$$

The first equation is a temporal reverse diffusion step before applying the manifold-constrained samplings. The second equation applies the manifold-constrained gradient $\gamma \frac{\partial}{\partial \mathbf{y}^{(t+1)}} \|\mathbf{y}_L - \mathbf{P} \hat{\mathbf{y}}\|_2^2$, where \mathbf{P} and $\bar{\mathbf{P}}$ is a masking matrix that selects the labeled nodes and unlabeled nodes, respectively. Here, $\hat{\mathbf{y}}$ is $\left(\mathbf{y}^{(t+1)} - \frac{1 - \bar{\alpha}_{t+1}}{\sqrt{1 - \bar{\alpha}_{t+1}}} \boldsymbol{\epsilon}_\theta(\mathbf{x}, \mathbf{y}^{(t+1)}, G, t + 1) \right) / \sqrt{\bar{\alpha}_{t+1}}$, and γ is a hyper-parameter. Following Chung et al. (2022), we set γ to $1 / \|\mathbf{y}_L - \mathbf{P} \hat{\mathbf{y}}\|_2^2$. The third equation is a consistency step. Additionally, we introduce a parameter λ to control the randomness; when we set λ to zero, the modified reverse step becomes deterministic. We describe the detailed sampling algorithm in Algorithm 2.

Algorithm 2 Manifold-constrained sampling

- 1: **Input:** Graph G , node attributes \mathbf{x} , labels \mathbf{y}_L , and temperature of randomness λ^2 .
 - 2: Get $\mathbf{y}^{(T)} \sim \mathcal{N}(\mathbf{y}^{(T)}; \mathbf{0}, \lambda^2 \mathbf{I})$ ▷ Initial sampling
 - 3: **for** $t = T - 1, \dots, 0$ **do**
 - 4: Get $\mathbf{z} \sim \mathcal{N}(\mathbf{z}; \mathbf{0}, \lambda^2 \mathbf{I})$
 - 5: $\mathbf{y}'^{(t)} \leftarrow \frac{1}{\sqrt{\alpha_t}} \left(\mathbf{y}^{(t+1)} - \frac{\beta_{t+1}}{\sqrt{1 - \bar{\alpha}_{t+1}}} \boldsymbol{\epsilon}_\theta(\mathbf{x}, \mathbf{y}^{(t+1)}, G, t + 1) \right) + \sigma_{t+1} \mathbf{z}$ ▷ Temporal reverse diffusion step
 - 6: $\hat{\mathbf{y}} \leftarrow \left(\mathbf{y}^{(t+1)} - \frac{1 - \bar{\alpha}_{t+1}}{\sqrt{1 - \bar{\alpha}_{t+1}}} \boldsymbol{\epsilon}_\theta(\mathbf{x}, \mathbf{y}^{(t+1)}, G, t + 1) \right) / \sqrt{\bar{\alpha}_{t+1}}$
 - 7: $\mathbf{y}_U^{(t)} \leftarrow \bar{\mathbf{P}} \left(\mathbf{y}'^{(t)} - \gamma \frac{\partial}{\partial \mathbf{y}^{(t+1)}} \|\mathbf{y}_L - \mathbf{P} \hat{\mathbf{y}}\|_2^2 \right)$ ▷ Manifold-constrained gradient
 - 8: Get $\mathbf{z} \sim \mathcal{N}(\mathbf{z}; \mathbf{0}, \lambda^2 \mathbf{I})$
 - 9: $\mathbf{y}_L^{(t)} \leftarrow \sqrt{\bar{\alpha}_t} \mathbf{y}_L + \sqrt{1 - \bar{\alpha}_t} \mathbf{z}$ ▷ Consistency step
 - 10: $\mathbf{y}^{(t)} \leftarrow \mathbf{y}_L^{(t)} \cup \mathbf{y}_U^{(t)}$
 - 11: **end for**
 - 12: **return** $\mathbf{y}_U^{(0)}$
-

C. Experimental details

In this section, we describe detailed experiment settings. The unique hyper-parameters of DPM-GSP are listed as follows.

- Number of diffusion steps (T).
- Unweighted mean squared error (unweighted MSE).

C.1. Inductive node classification

Inductive node classification (Pubmed, Cora, Citeseer, and DBLP). In this experiment, we set the hidden dimension and the number of layers in the GNN similarly to the experimental settings in [Qu et al. \(2022\)](#).

- **GCN:** We set the hidden dimensions and the number of layers to 16 and two, respectively. Here, we use ReLU ([Nair & Hinton, 2010](#)) as the activation function.
- **GraphSAGE:** We set the hidden dimensions to 80. The number of layers is determined through a grid search within the range $\{2, 4\}$. Here, we use ReLU ([Nair & Hinton, 2010](#)) as the activation function.
- **GAT:** We set the hidden dimensions and the number of heads to 256 and four, respectively. The number of layers is determined through a grid search within the range $\{2, 4\}$. Here, we use ELU ([Clevert et al., 2015](#)) as the activation function. We include an optional linear skip connection between each layer.

The obtained node representations are then passed through the MLP, with the number of layers determined through a grid search within the range of $\{1, 2\}$. Additional hyperparameter search ranges for DPM-GSP, CLGNN, and SPN can be found in [Table 7](#), [Table 8](#), and [Table 9](#), respectively. For edge temperatures in the SPN, we use the values reported by [Qu et al. \(2022\)](#). In the case of the base GNN, the grid search ranges for the learning rate and weight decay are the same as the search ranges of CLGNN. We use Adam ([Kingma & Ba, 2014](#)) to optimize DPM-GSP, SPN, CLGNN, and GNN. In the case of GMNN, we use the results reported by [Qu et al. \(2022\)](#).

Table 7. Hyper-parameters search ranges of DPM-GSP for Pubmed, Cora, and Citeseer.

Network	learning rate	weight decay	T	unweighted MSE
GCN	0 for DBLP and $\{0.005, 0.001, 0.0005\}$ for others	$\{0.003, 0.001, 0.0005\}$	$\{40, 80\}$	$\{\text{True}, \text{False}\}$
GraphSAGE	0 for DBLP and $\{0.001, 0.0005\}$ for others	$\{0.001, 0.0005\}$	$\{40, 80\}$	$\{\text{True}, \text{False}\}$
GAT	0 for DBLP and $\{0.001, 0.0005, 0.0001\}$ for others	$\{0.001, 0.0005, 0.0001\}$	$\{40, 80\}$	$\{\text{True}, \text{False}\}$

Table 8. Hyper-parameters search ranges of CLGNN for Pubmed, Cora, and Citeseer.

Models	learning rate	weight decay	number of Monte Carlo samples
GCN	$\{0.01, 0.005, 0.001\}$	$\{0.003, 0.001, 0.0005\}$	$\{5, 10\}$
GraphSAGE	$\{0.01, 0.005, 0.001\}$	$\{0.001, 0.0005\}$	$\{5, 10\}$
GAT	$\{0.01, 0.005, 0.001\}$	$\{0.001, 0.0005, 0.0001\}$	$\{5, 10\}$

Table 9. Hyper-parameters search ranges of SPN for Pubmed, Cora, and Citeseer.

Network	learning rate (node GNN)	learning rate (edge GNN)	weight decay
GCN	$\{0.01, 0.005\}$	$\{0.01, 0.005\}$	$\{0.003, 0.001, 0.0005\}$
GraphSAGE	$\{0.005, 0.001\}$	$\{0.005, 0.001\}$	$\{0.001, 0.0005\}$
GAT	$\{0.005, 0.001\}$	$\{0.005, 0.001, 0.0005\}$	$\{0.001, 0.0005, 0.0001\}$

Inductive node classification (PPI). In this experiment, we set the number of layers in the GNN similarly to the experimental settings in [Qu et al. \(2022\)](#).

- **GCN:** We set the hidden dimensions and the number of layers to 1024 and two, respectively. Here, we use ReLU (Nair & Hinton, 2010) as the activation function. We also include the linear skip connection between each layer.
- **GraphSAGE:** We set the hidden dimensions and the number of layers to 1024 and four, respectively. Here, we use ReLU (Nair & Hinton, 2010) as the activation function. We also include the linear skip connection between each layer.
- **GAT:** We set the hidden dimensions, the number of heads, and the number of layers to 256, four, and four, respectively. Here, we use ELU (Clevert et al., 2015) as the activation function. We also include the linear skip connection between each layer.

The obtained node representations are then passed through the three-layer MLP. Additional hyperparameter search ranges for DPM-GSP, and CLGNN can be found in Table 10 and Table 11, respectively. Since this task involves the loss for 121 labels, we set the learning rate low. In the case of the base GNN, the grid search ranges for the learning rate and weight decay are the same as the search ranges of CLGNN. We use Adam (Kingma & Ba, 2014) to optimize DPM-GSP, CLGNN, and base GNN. In the case of GMNN and SPN, we use the results reported by Qu et al. (2022).

Table 10. Hyper-parameters search ranges of DPM-GSP for PPI.

Network	learning rate	weight decay	T	unweighted MSE
GCN, GraphSAGE, and GAT	{0.0003, 0.0001}	0	{80, 200}	True

Table 11. Hyper-parameters search ranges of CLGNN for PPI.

Network	learning rate	weight decay	number of Monte Carlo samples
GCN, GraphSAGE, and GAT	{0.0003, 0.0001}	0	5

C.2. Transductive node classification

The unique hyper-parameters of semi-supervised DPM-GSP are listed as follows.

- Size of the buffer (K).
- Number of iterations in expectation step (N_1).
- Number of iterations in maximization step (N_2).
- Number of initial iterations (N_2^{initial}): During this iteration, the maximization step utilizes the buffer initialized by the mean-field GNN.
- Temperature of manifold-constrained sampling in constructing buffer (λ_{buffer}): Following the temperature annealing approach of Qu et al. (2019), we also control the sampling temperature λ_{buffer} in obtaining y_U for buffer construction.

Transductive node classification (Pubmed, Cora, and Citeseer). In this experiment, we set the hidden dimensions, and the number of layers as follows:

- **GCN and GraphSAGE:** We set the hidden dimensions and the number of layers to 64 and two, respectively. Here, we use ReLU (Nair & Hinton, 2010) as the activation function. We apply dropout with a probability of 0.5.
- **GAT:** We set the hidden dimensions, the number of heads, and the number of layers to eight, eight, and two, respectively. Here, we use ELU (Clevert et al., 2015) as the activation function. We include an optional linear skip connection between each layer. We apply dropout with a probability of 0.5.

The obtained node representations are then passed through the one-layer MLP. Additional hyperparameter search ranges for DPM-GSP, and CLGNN can be found in Table 12 and Table 13, respectively. In the case of the base GNN, the grid search ranges for the learning rate and weight decay are the same as the search ranges of CLGNN. We use Adam (Kingma

& Ba, 2014) to optimize DPM-GSP, CLGNN, and base GNN. We also use hyper-parameters reported by Qu et al. (2019) in optimizing the GMNN. In the case of G3NN, LCM, and LP-baSed methods, we use the results reported by Ma et al. (2019a), Wang et al. (2021), and Bo et al. (2022), respectively.

Table 12. Hyper-parameters search ranges of DPM-GSP for Pubmed, Cora, and Citeseer (semi-supervised learning).

Models	lr	weight_decay	T	unweighted MSE	K	N_1	N_2	N_2^{initial}	λ_{buffer}
GCN and GraphSAGE	{0.01, 0.005, 0.001}	{0.01, 0.005, 0.001}	80	True	50	5	100	1000	{0.3, 0.5, 1}
GAT	{0.01, 0.005, 0.001, 0.0005}	{0.01, 0.005, 0.001}	80	True	50	5	100	2000	{0.3, 0.5, 1}

Table 13. Hyper-parameters search ranges of CLGNN for Pubmed, Cora, and Citeseer (semi-supervised learning).

Models	learning rate	weight decay	number of Monte Carlo samples
GCN and GraphSAGE	{0.05, 0.01, 0.005}	{0.01, 0.005, 0.001}	{5, 10}
GAT	{0.01, 0.005, 0.001}	{0.01, 0.005, 0.001}	{5, 10}

Transductive node classification (Amazon Photo and Computer). In this experiment, we set the hidden dimensions, and the number of layers as follows:

- **GCN and GraphSAGE:** We set the hidden dimensions and the number of layers to 128 and two, respectively. Here, we use ReLU (Nair & Hinton, 2010) as the activation function. We apply dropout with a probability of 0.5.
- **GAT:** We set the hidden dimensions, the number of heads, and the number of layers to 16, eight, and two, respectively. Here, we use ELU (Clevert et al., 2015) as the activation function. We apply dropout with a probability of 0.5.

The obtained node representations are then passed through the one-layer MLP. Additional hyperparameter search ranges for DPM-GSP, CLGNN, and GMNN can be found in Table 14 and Table 15, and Table 16, respectively. In the case of the base GNN, the grid search ranges for the learning rate and weight decay are the same as the search ranges of CLGNN. We use Adam (Kingma & Ba, 2014) to optimize DPM-GSP, CLGNN, GMNN, and base GNN. In the case of LP-based methods, we use the results reported by Bo et al. (2022).

Table 14. Hyper-parameters search ranges of DPM-GSP for Amazon Photo and Computer (semi-supervised learning).

Models	lr	weight_decay	T	unweighted MSE	K	N_1	N_2	N_2^{initial}	λ_{buffer}
GCN	{0.005, 0.001}	{0.005, 0.001, 0.0005}	80	True	50	5	100	2000	{0.1, 0.3, 0.5, 1}
GraphSAGE and GAT	{0.001, 0.0005}	{0.001, 0.0005, 0.0001}	80	True	50	5	100	2000	{0.1, 0.3, 0.5, 1}

Table 15. Hyper-parameters search ranges of CLGNN for Amazon Photo and Computer (semi-supervised learning).

Models	learning rate	weight decay	number of Monte Carlo samples
GCN	{0.005, 0.001}	{0.005, 0.001, 0.0005}	5
GraphSAGE and GAT	{0.005, 0.001}	{0.001, 0.0005, 0.0001}	5

Table 16. Hyper-parameter search ranges of GMNN for Amazon Photo and Computer (semi-supervised learning).

learning rate	weight decay	hidden dimension	annealing parameter λ
{0.005, 0.001}	{0.005, 0.001, 0.0005}	128	{0.1, 0.3, 0.5, 1}

Transductive node classification (Cornell, Wisconsin, and Texas). In this experiment, we set the hidden dimensions, and the number of layers as follows:

- **GCN and GraphSAGE:** We set the hidden dimensions and the number of layers to 64 and one, respectively. Here, we use ReLU (Nair & Hinton, 2010) as the activation function. We apply dropout with a probability of 0.5.

- **GAT:** We set the hidden dimensions, the number of heads, and the number of layers to eight, eight, and one, respectively. Here, we use ELU (Clevert et al., 2015) as the activation function. We apply dropout with a probability of 0.5.

The obtained node representations are then passed through the one-layer MLP. We provide the additional hyper-parameters search ranges of DPM-GSP, CLGNN, and GMNN in Table 17, Table 18 and Table 19, respectively. We use Adam (Kingma & Ba, 2014) to optimize DPM-GSP, CLGNN, GMNN, and base GNN. In the case of the base GNN, the grid search ranges for the learning rate and weight decay are the same as the search ranges of CLGNN.

Table 17. Hyper-parameters search ranges of DPM-GSP for Cornell, Wisconsin, and Texas (semi-supervised learning).

Models	lr	weight_decay	T	unweighted MSE	K	N_1	N_2	N_2^{initial}	λ_{buffer}
GCN, GraphSAGE, and GAT	{0.01, 0.005, 0.001}	{0.01, 0.005, 0.001}	80	True	50	5	50	1000	{0.1, 0.3, 0.5, 1}

Table 18. Hyper-parameters search ranges of CLGNN for Cornell, Wisconsin, and Texas (semi-supervised learning).

Models	learning rate	weight decay	number of Monte Carlo samples
GCN, GraphSAGE, and GAT	{0.01, 0.005, 0.001}	{0.01, 0.005, 0.001}	{5, 10}

Table 19. Hyper-parameter search ranges of GMNN for Cornell, Wisconsin, and Texas (semi-supervised learning).

learning rate	weight decay	hidden dimension	annealing parameter λ
{0.01, 0.005, 0.001}	{0.01, 0.005, 0.001}	64	{0.1, 0.3, 0.5, 1}

C.3. Graph algorithmic reasoning

In this section, we consider solving graph algorithmic reasoning tasks with DPM-GSP. Here, the attributes and the targets are associated with edges, i.e., $\mathbf{x} = \{x_i : i \in \mathcal{E}\}$ and $\mathbf{y} = \{y_i : i \in \mathcal{E}\}$. If the targets \mathbf{y} are discrete, we relax them into a one-hot vector to yield continuous values. The forward and reverse diffusion scheme is the same as that in the Section 3.1, i.e., injects and eliminates Gaussian noise on the edge targets.

The parameterization of the reverse process is similar to the parameterization of the energy-based model of IREM (Du et al., 2022). Specifically, the noisy edge target $\mathbf{y}^{(t)}$ is updated as follows. First, the noisy edge targets $\mathbf{y}^{(t)}$ and edge features x are concatenated and passed through the GINEConv layer, which aggregates the neighboring node features and edge features to output the node representation (Hu et al., 2020). Here, the number of GINEConv layers and hidden dimensions are three and 128, respectively. The node features are initialized to zero. After applying each GINEConv layer, we add the time embedding vector to the node representation. Then, we concatenate a pair of final node representations and noisy targets for the given edges and then apply a two-layer MLP to obtain $\mathbf{y}^{(t-1)}$.

In contrast to the node classification, we introduce randomness in the reverse process, i.e., we use the stochastic reverse process for obtaining $\mathbf{y}^{(0)}$. This approach is consistent with the IREM, which also includes randomness. The detailed hyper-parameters are reported in Table 20. We use Adam (Kingma & Ba, 2014) to optimize DPM-GSP. The reported results of other baselines are taken from Du et al. (2022).

Table 20. Hyper-parameters of DPM-GSP for graph algorithmic reasoning.

learning rate	weight decay	T	unweighted MSE	temperature of reverse process
{0.0004, 0.0001}	{1e-6, 1e-5}	{50, 100}	True	{0.3, 0.5, 1}